

Scalable Segmentation for Ultra-High-Resolution Brain MR Images

Xiaoling Hu^{1,†}, Peirong Liu¹, Dina Zemlyanker¹, Jonathan Williams Ramirez¹,
Oula Puonti^{1,2}, Juan Eugenio Iglesias^{1,3,4}

¹Massachusetts General Hospital and Harvard Medical School

²Danish Research Centre for Magnetic Resonance, Copenhagen University Hospital

³Hawkes Institute, University College London

⁴Computer Science and AI Laboratory, Massachusetts Institute of Technology

Abstract

Although deep learning has shown great success in 3D brain MRI segmentation, achieving accurate and efficient segmentation of ultra-high-resolution brain images remains challenging due to the lack of labeled training data for fine-scale anatomical structures and high computational demands. In this work, we propose a novel framework that leverages easily accessible, low-resolution coarse labels as spatial references and guidance, without incurring additional annotation cost. Instead of directly predicting discrete segmentation maps, our approach regresses per-class signed distance transform maps, enabling smooth, boundary-aware supervision. Furthermore, to enhance scalability, generalizability, and efficiency, we introduce a *scalable class-conditional segmentation* strategy, where the model learns to segment one class at a time conditioned on a class-specific input. This novel design not only reduces memory consumption during both training and testing, but also allows the model to generalize to unseen anatomical classes. We validate our method through comprehensive experiments on both synthetic and real-world datasets, demonstrating its superior performance and scalability compared to conventional segmentation approaches. Code is available at: <https://github.com/HuXiaoling/HighSeg>.

1 Introduction

Brain MRI segmentation is one of the fundamental tasks in neuroimaging, playing a key role in various downstream analyses such as tumor diagnosis and monitoring [65, 48, 44, 37], volumetric and shape analyses [33, 22, 26], and more. Though considered the gold standard, manual segmentation requires specialized domain expertise and is typically irreproducible. The time-consuming annotation process further makes manual segmentations impractical, especially for large and ultra-high-resolution datasets. To overcome these challenges, efforts have been made on developing methods for automated segmentation of brain scans [1, 28, 49, 9].

Over the last decade, supervised deep learning methods have been dominant for both natural image segmentation [45, 10, 11, 12, 50] and medical image segmentation [55, 49, 35, 5, 37], thanks to the availability of high-quality, labeled data. However, deep learning models often struggle in contexts where there is limited number of high-quality labels, especially in clinical settings when such labels are difficult to obtain. In addition to the scarcity of labeled data and the complexity of brain anatomical structures, the significant heterogeneity and variability, including the orientation of images (axial, coronal, or sagittal), slice spacing, and in-plane resolution, of brain scans impose additional

[†] Email: Xiaoling Hu (xihu3@mgh.harvard.edu)

challenges for brain image segmentation. Moreover, the diversity of imaging protocols, which include various sequences and modalities designed to capture different tissue properties, results in substantial variations in intensity distributions. These variations can severely impact the performance of supervised CNNs [67, 8], limiting their accuracy and robustness in brain scan segmentation.

Ultra-high-resolution 3D brain imaging, such as *ex vivo* MRI with near 100-micron isotropic resolution, offers unprecedented anatomical details and enables visualization of fine-grained cortical and subcortical structures [38]. However, this high fidelity comes at the cost of significantly increased computational and algorithmic complexity. The volumetric size of these scans often exceeds hundreds of millions of voxels, making direct training and inference with conventional deep learning models difficult due to memory constraints. Also, the fine-scale structures present in such data demand high-precision boundary delineation, which is challenging for models trained on lower-resolution images. Furthermore, manual annotation at ultra-high resolution is prohibitively time-consuming and inconsistent, making large-scale, fully labeled datasets rare. Together, these factors make ultra-high-resolution brain image segmentation a uniquely demanding task that requires new approaches in model design, supervision strategies, and data scalability.

In this paper, we seek to circumvent the limitations of traditional segmentation pipelines, which typically rely on dense, voxel-wise annotations at full resolution and predict all classes simultaneously – resulting in high memory consumption and limited scalability, particularly when segmenting dozens of anatomical structures. To address these challenges, we propose a geometry-aware framework that leverages easily accessible segmentations obtained from low-resolution scans as auxiliary guidance. Rather than directly predicting discrete segmentation masks, our method regresses per-class signed distance transform maps. To further improve the quality of the regressed distance fields, we impose additional regularization terms, including a *gradient norm* loss that encourages the regressed distance maps to approximate true signed distance functions near object boundaries, and a *total variation* (TV) loss that promotes local smoothness by penalizing abrupt spatial fluctuations. These constraints guide the network toward producing geometrically plausible and topologically consistent signed distance maps, which in turn support more accurate and stable segmentation.

Furthermore, to improve computational scalability and flexibility, we introduce a novel *scalable class-conditional segmentation* mechanism. By conditioning the input on a single sampled class, the model can focus on learning localized features relevant to the target class without sacrificing full segmentation coverage. This strategy not only reduces memory but also facilitates generalization to previously unseen classes by decoupling class-wise learning and reducing inter-class interference. We validate the effectiveness of our approach through comprehensive experiments on both synthetic and real-world datasets, demonstrating its superiority over conventional multi-class segmentation methods in terms of accuracy, efficiency, scalability, and generalizability.

We summarize our key contributions as follows:

1. We propose a novel signed distance transform (SDF) regression strategy that enables continuous, boundary-aware learning and generalizes well across spatial resolutions.
2. We design a *scalable class-conditional segmentation* framework that allows class-wise prediction conditioned on a reference low-resolution segmentation, improving both memory efficiency and model flexibility.
3. We demonstrate that our method outperforms conventional segmentation approaches in both accuracy and scalability across diverse datasets.

2 Related Works

Deep learning based medical image segmentation. In the last decade, deep learning methods (CNNs) have provided state-of-the-art accuracy in (medical) image segmentation [55, 45, 10, 11, 12, 50, 37]. The UNet architecture [55] and its variants [35, 9, 49] have been one of the most popular methods for medical image segmentation. FCN [45] transforms classification CNNs [42, 60, 30] to fully-convolutional NNs by replacing fully connected layers with fully convolutional layers. By doing this, FCN transfers the success of classification tasks [42, 60, 63] to segmentation tasks. Deeplab methods (v1-v2) [10, 11] add another fully connected Conditional Random Field (CRF) after the last CNN layer to make use of global information instead of using CRF as post-processing. Moreover, dilated/atrous convolutions were introduced in Deeplab v3 [12] to increase the receptive field and

make better use of context information, resulting in better performance. Numerous adaptations have been proposed for brain-specific segmentation tasks, including multi-atlas segmentation [34], patch-based models [29], and whole-volume architectures such as QuickNAT [57] and FastSurfer [31], which aim to balance speed and accuracy. More recent approaches have explored self-supervised pretraining [43], domain adaptation [25], and attention mechanisms [54] to enhance robustness across datasets and populations.

Despite these successful applications, several challenges remain, especially when scaling to ultra-high-resolution brain images. First, the fine-grained anatomical details in such volumes require models to preserve subtle boundary information while maintaining spatial coherence. Second, the large voxel count in ultra-high-resolution data imposes substantial memory and computational burdens. These challenges highlight the need for segmentation methods that are both computationally efficient and robust to limited or coarse supervision, motivating the design of more scalable and geometry-aware frameworks.

Distance transform. For image segmentation tasks, most existing deep neural network (DNN) based methods use binary or multi-label masks as ground truth to supervise the training of the networks. Distance transform maps (DTM) [59] offer an alternative to classical ground truth. For example, the distance transform can transform a binary mask into grayscale images, termed a distance transform map, where the pixel values denote the distances to the closest boundary. To distinguish the inside and outside of objects, the signed distance function (SDF) [51, 53, 7, 14, 15, 36] has been proposed. Over the past few years, researchers have tried to incorporate the distance transform maps of image segmentation labels into deep neural networks. Distance transform maps can be an alternative for supervising the training of CNNs [68, 47, 2, 4].

Instead of predicting the segmentation mask directly, we want to regress a signed distance map. Distance transform [56, 18, 19] transforms the original image into a map of the same size, with the pixel value denoting the distance from the pixel to the foreground boundary. The distance map is known to encode the geometric structures of instance objects, which drives us to design a geometry-aware model, with the help of a geometric prior from the low-resolution map.

Scalable image segmentation. Scalable image segmentation has received growing attention as datasets increase in resolution, size, and label complexity. Traditional segmentation methods typically predict all classes simultaneously using dense, multi-channel outputs, which becomes computationally prohibitive in ultra-high-resolution images or when scaling to a large number of anatomical classes. To address this, recent work has explored class-wise or conditional segmentation strategies. In natural image domains, Panoptic FPN [40] tackles scalability by separating instance-level and class-level predictions, while more recent prompt-based models like Segment Anything [41] use conditional inputs to guide segmentation. Class-conditional [62, 13, 70] or modular approaches [66, 71] allow models to focus on one structure at a time, improving generalizability to rare or unseen classes. Incremental segmentation [6, 24, 23] and few-shot medical segmentation [64, 52, 20] further demonstrate how conditioning enables label-efficient learning.

Our work builds upon these ideas by introducing a *scalable class-conditional segmentation* framework that enables efficient and generalizable segmentation of ultra-high-resolution brain images without requiring full multi-class predictions during training. By conditioning the model on a single target class at a time, we significantly reduce memory consumption and improve scalability, allowing the model to focus on localized anatomical structures without interference from competing class labels. This per-class supervision scheme not only simplifies training but also promotes modularity, making it well-suited for incorporating new or rare anatomical classes without retraining the entire model.

3 Methods

Preliminaries. We focus on supervised segmentation frameworks for ultra-high-resolution brain images, where the model is trained on a set of triplets (I_H, S_l, S_H) . Here, $I_H \in \mathbb{R}^{1 \times D \times H \times W}$ denotes the ultra-high-resolution input image, $S_H \in \mathbb{N}^{1 \times D \times H \times W}$ is the corresponding ultra-high-resolution ground-truth segmentation used for direct supervision, and $S_l \in \mathbb{N}^{1 \times D' \times H' \times W'}$ is a coarse, low-resolution segmentation map that serves as a spatial reference. We are thus seeking to train a neural network \mathbf{F}_θ with parameters θ , such that, $\hat{S}_H = \mathbf{F}_\theta(I_H | S_l)$, which will be simplified as $\hat{S}_H = \mathbf{F}_\theta(I_H)$ in the rest of this article.

The remainder of this section is organized as follows. In Section 3.1, we introduce the baseline setting of supervised segmentation using low-resolution annotations as auxiliary spatial guidance, which serves as the basis of our framework. Section 3.2 describes our geometry-aware formulation based on regressing signed distance transform maps instead of discrete segmentation labels, enabling smooth and boundary-sensitive supervision. In Section 3.3, we present the proposed *scalable class-conditional segmentation* strategy, which allows the model to efficiently scale to a large number of anatomical structures and generalize to unseen classes through per-class conditional training.

3.1 Supervised Segmentation with Low-Resolution Guidance

3.1.1 Naive Supervised Segmentation

A straightforward approach to segmenting ultra-high-resolution brain images is to directly train a segmentation network using the raw high-resolution image $I_H \in \mathbb{R}^{1 \times D \times H \times W}$ and its corresponding voxel-wise ground-truth segmentation $S_H \in \mathbb{N}^{1 \times D \times H \times W}$. In this naive setting, the network is supervised with a standard multi-class cross-entropy loss or Dice loss to predict the full-resolution segmentation map. While conceptually simple, this approach poses significant computational and practical challenges. The large volume size of I_H leads to high memory consumption during training and inference, often necessitating aggressive patching strategies that may compromise spatial context [69, 38]. Additionally, acquiring dense high-resolution labels S_H is labor-intensive and rarely feasible at scale, making this fully supervised paradigm both resource-intensive. We use this naive setup as a baseline, and aim for more scalable and label-efficient alternatives, as presented below.

3.1.2 Leveraging Low-Resolution Segmentation as Guidance

Beyond training the naive supervised segmentation network, we propose to leverage the coarse, low-resolution segmentation S_l as additional guidance, which is easily obtained by using automatic tools, such as SynthSeg [3]. The low-resolution segmentation S_l serves two purposes in the learning process. First, S_l can be used as prior information to guide the segmentation. Specifically, S_l is upsampled to match the resolution of I_H using trilinear interpolation on the one-hots, $S_{up} = \text{Upsample}(S_l)$. S_{up} is then concatenated with the input image to form an augmented input, $\tilde{I} = \text{Concat}(I, S_{up}) \in \mathbb{R}^{(1+C) \times D \times H \times W}$, where C is the number of semantic classes present in the segmentation map.

Second, the low-resolution reference is also used to enforce semantic consistency. Given the network prediction $\hat{S}_H = \mathbf{F}_\theta(\tilde{I})$, we downsample the ultra-high-resolution prediction to obtain \hat{S}_l at the same spatial resolution as S_l , $\hat{S}_l = \text{Downsample}(\hat{S}_H)$. A consistency loss is then applied to ensure that the downsampled prediction agrees with the reference segmentation, $\mathcal{L}_{\text{cons}} = \text{Dice}(\hat{S}_l, S_l)$.

For the main segmentation task, we apply a voxel-wise Dice loss between the ultra-high-resolution prediction and the ground-truth segmentation, $\mathcal{L}_{\text{seg}} = \text{Dice}(\hat{S}_H, S_H)$.

The total loss is a weighted sum of the segmentation and consistency terms:

$$\mathcal{L}_{\text{total}} = \mathcal{L}_{\text{seg}} + \lambda_{\text{cons}} \mathcal{L}_{\text{cons}}, \quad (1)$$

where λ_{cons} is a hyperparameter that controls the influence of the consistency loss.

In order to reduce the computational cost, a patch-based training strategy is commonly adopted. This, however, will also introduce non-trivial challenges (see Figure 1). In particular, aligning ultra-high-resolution image patches with their corresponding regions in the low-resolution reference S_l requires careful handling of spatial coordinates and affine transformations. Misalignment during cropping can lead to incorrect auxiliary input and reduce the effectiveness of consistency regularization.

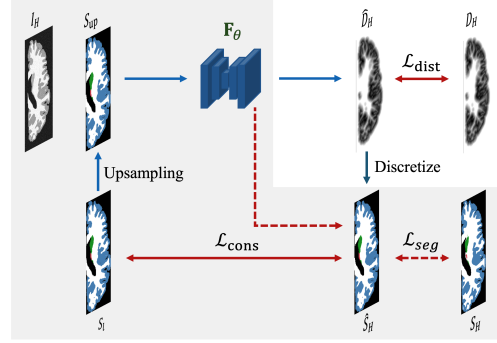


Figure 1: Beyond the classical supervision \mathcal{L}_{seg} (dashed line), we impose additional $\mathcal{L}_{\text{cons}}$ to enforce the spatial consistency (Sec. 3.1). In addition, instead of predicting the segmentation maps directly (shaded in gray), we regress the signed distance maps (D_H) (Sec. 3.2).

Direct segmentation often relies on hard class assignments or discrete boundaries, which can result in unstable optimization, especially near ambiguous or poorly defined borders. Since each voxel is treated as an independent categorical decision, the model may struggle to learn consistent spatial patterns, particularly at fine structural interfaces. This pixel-wise classification paradigm also lacks an explicit encoding of geometry or spatial continuity, making it difficult for the model to preserve global anatomical geometry or smoothness. As a result, direct segmentation often produces outputs with jagged edges, disconnected components, or topology violations. These limitations motivate the need for alternative representations, such as signed distance maps, which provide a more continuous and geometry-aware form of supervision.

3.2 Regressing Signed Distance Transforms

Definition of distance transform. Given a 3D multi-class segmentation label map $S : \Omega \subset \mathbb{R}^3 \rightarrow \{0, 1, \dots, C-1\}$, where each voxel $x \in \Omega$ is assigned a class label, the signed distance map $D^c : \Omega \rightarrow \mathbb{R}$ for each class $c \in \{1, \dots, C-1\}$ is defined as:

$$D^c(x) = \begin{cases} -\min_{y \in \partial\Omega^c} \|x - y\|_2, & \text{if } x \in \Omega^c \\ \min_{y \in \partial\Omega^c} \|x - y\|_2, & \text{if } x \notin \Omega^c \end{cases}$$

where, $\Omega^c = \{x \in \Omega \mid S(x) = c\}$ is the foreground region for class c , $\partial\Omega^c$ denotes the boundary of Ω^c , and $\|\cdot\|_2$ is the Euclidean distance in 3D space. The full multi-class signed distance map can be represented as a tensor $D \in \mathbb{R}^{C \times D \times H \times W}$, where D^c corresponds to the distance map for class c .

Instead of directly predicting discrete segmentation labels, regressing distance transform maps provides several key advantages, particularly in the context of high-resolution and boundary-sensitive segmentation tasks. First, distance maps offer a continuous representation of anatomical structures, capturing spatial proximity to boundaries more effectively than discrete labels [58]. This leads to smoother gradients during training and encourages the network to focus on boundary precision, which is important for fine-scale brain structures. Second, distance regression is inherently more robust to label noise and misalignment, especially when supervision is derived from coarsely annotated or low-resolution sources [27, 36]. These properties make distance transform regression a powerful alternative to conventional segmentation approaches, particularly for ultra-high-resolution medical image analysis.

We regress signed distance transforms (SDFs) for each semantic class to enable geometry-aware segmentation of ultra-high-resolution images. This continuous representation encodes boundary proximity and facilitates smoother learning compared to discrete label prediction. The network \mathbf{F}_θ regresses ultra-high-resolution distance maps, $\hat{D}_H = \mathbf{F}_\theta(\tilde{I}) \in \mathbb{R}^{C \times D \times H \times W}$. Supervision is applied via an ℓ_1 loss against the distance transforms computed from the ultra-high-resolution label S_H , $\mathcal{L}_{\text{dist}} = \|\hat{D}_H - D_H\|_1$. By converting the regressed distance map \hat{D}_H to (soft) segmentation map,

$$\hat{S}_H^c(v) = \frac{\exp(-\hat{D}_H^c(v)/\tau)}{\sum_{c'=1}^C \exp(-\hat{D}_H^{c'}(v)/\tau)}, \quad \forall c \in \{1, \dots, C\}. \quad (2)$$

Here, $D_H^c(v)$ denotes the predicted signed distance at voxel v for class c , τ is the temperature parameter (controls the sharpness of the distance-to-probability mapping), $\hat{S}_H^c(v) \in [0, 1]$ is the probability that voxel v belongs to class c , and the output $\hat{S}_H \in \mathbb{R}^{C \times D \times H \times W}$ is a probabilistic segmentation map.

Regularization on the regressed signed distance map. To improve the smoothness and geometric consistency of the predicted signed distance maps, we incorporate two regularization terms during training, a *gradient norm (GN)* loss \mathcal{L}_∇ , and a *total variation (TV)* loss, \mathcal{L}_{TV} . These regularizers are applied directly to the regressed signed distance fields, which are first clipped to a predefined range to prevent instability from extreme values far from object boundaries.

The *gradient norm* loss encourages the predicted distance maps to approximate a unit gradient norm near object surfaces, aligning with the theoretical property of true signed distance functions [46]. Formally,

$$\mathcal{L}_\nabla(\hat{D}_H) = \frac{1}{|\Omega|} \sum_{v \in \Omega} \left(\|\nabla \hat{D}_H(v)\|_2 - 1 \right)^2. \quad (3)$$

Meanwhile, the *total variation* loss penalizes abrupt local changes in the distance fields, suppressing high-frequency noise and promoting spatial smoothness. Together, these regularization terms act as geometry-aware constraints, guiding the network toward more stable, realistic, and generalizable predictions. The \mathcal{L}_{TV} is defined as,

$$\mathcal{L}_{\text{TV}}(\hat{D}_H) = \frac{1}{|\Omega|} \sum_{v \in \Omega} \sqrt{\sum_{i=1}^3 \left(\nabla_i \hat{D}_H(v) \right)^2}. \quad (4)$$

To encourage resolution consistency, the predicted segmentation maps are downsampled and compared with the low-resolution reference, $\hat{S}_l = \text{Downsample}(\hat{S}_H)$, $\mathcal{L}_{\text{cons}} = \text{Dice}(\hat{S}_l, S_l)$.

The total loss combines the distance regression and consistency terms,

$$\mathcal{L}_{\text{total}} = \mathcal{L}_{\text{dist}} + \lambda_{\text{gn}} \mathcal{L}_{\nabla}(\hat{D}_H) + \lambda_{\text{tv}} \mathcal{L}_{\text{TV}}(\hat{D}_H) + \lambda_{\text{cons}} \mathcal{L}_{\text{cons}}, \quad (5)$$

where λ_{gd} , λ_{tv} are weighting coefficients for each regularize, and λ_{cons} weights the contribution of the low-resolution constraint. The architecture is illustrated in Figure 1.

At inference time, segmentation is recovered by assigning each voxel to the class with the minimum signed distance, $\hat{S}_H(v) = \arg \min_c \hat{D}_H^c(v)$.

3.3 Scalable Class-Conditional Segmentation (SCCS)

Traditional segmentation frameworks are typically designed to predict all semantic classes simultaneously using a multi-channel output, with each channel corresponding to a distinct label. While effective for low- to moderate-resolution images with a limited number of classes, this design becomes increasingly inefficient and memory-intensive when applied to ultra-high-resolution volumes or segmentation tasks involving a large number of anatomical structures. The need to compute and store full-resolution predictions for every class not only imposes significant computational burdens but also limits the model’s scalability and flexibility. To address these limitations, we propose a *scalable class-conditional segmentation* strategy. Instead of generating dense predictions for all classes at once, the model is trained to focus on one class at a time, conditioned on a class-specific input. This decouples the segmentation problem across classes, significantly reduces memory requirements, and allows for flexible extension to new or unseen classes without retraining the entire model.

During training, we randomly sample a class $c \in \{1, \dots, C\}$ and extract its corresponding binary mask from the low-resolution reference segmentation S_l . This binary mask is then upsampled to match the resolution of the input image, $M_{\text{up}}^c = \text{Upsample}(\mathbb{1}_{S_l=c})$, and concatenated with the high-resolution image I to form a class-conditioned input, $\tilde{I}^c = \text{Concat}(I, M_{\text{up}}^c)$, where $\tilde{I}^c \in \mathbb{R}^{(1+1) \times D \times H \times W}$ includes both the raw image and the class-specific guidance channel. This class-specific conditioning guides the network’s attention toward the spatial regions relevant to class c , thereby enabling more focused learning.

The model \mathbf{F}_{θ} is trained to output the corresponding class segmentation prediction, $\hat{S}_H^c = \mathbf{F}_{\theta}(\tilde{I}^c) \in \mathbb{R}^{1 \times D \times H \times W}$, where \hat{S}_H^c represents the predicted probability maps for classes c . This design allows the network to benefit from class-specific spatial priors while preserving the ability to learn inter-class relationships and predict the entire label space at once. We apply a binary cross-entropy loss between the prediction and the ultra-high-resolution binary mask for class c , $\mathcal{L}_{\text{seg}}^c = \text{BCE}(\hat{S}_H^c, \mathbb{1}_{S_H=c})$.

To enforce consistency with the low-resolution reference segmentation, we also downsample the prediction and compare it to the original low-resolution reference mask, $\hat{S}_l^c = \text{Downsample}(\hat{S}_H^c)$, $\mathcal{L}_{\text{cons}}^c = \text{BCE}(\hat{S}_l^c, \mathbb{1}_{S_l=c})$. The total loss is given by,

$$\mathcal{L}_{\text{total}}^c = \mathcal{L}_{\text{seg}}^c + \lambda_{\text{cons}} \mathcal{L}_{\text{cons}}^c. \quad (6)$$

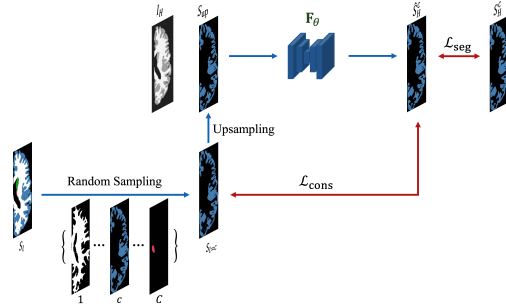


Figure 2: Training overview of the *scalable class-conditional segmentation* (Sec. 3.3).

Scalable multi-class aggregation from class-specific predictions. At inference time, the model is applied for each individual class c using a class-conditioned input \tilde{I}^c , which includes the image and the class-specific conditioning signal. The model produces a single-channel response map $\hat{S}^c \in \mathbb{R}^{1 \times D \times H \times W}$, indicating the probability that each voxel belongs to class c . After looping through all classes, the individual response maps are stacked to form a multi-class prediction volume. The final segmentation $\hat{S}_H(v)$ is then obtained by assigning each voxel v the label of the class with the highest response, $\hat{S}_H(v) = \arg \max_c \hat{S}^c(v)$.

Predicting one class at a time enables the model to scale efficiently to a large number of anatomical structures, which is particularly valuable when working with ultra-high-resolution brain images where memory and annotation constraints are significant. Moreover, it enables smoother generalization to unseen structures by leveraging class-aware contextual cues from the low-resolution reference. This framework decouples the segmentation task across classes, enabling ultra-high-resolution training with limited resources and making the model scalable to dozens or hundreds of classes without architectural changes.

4 Experiments

We conduct comprehensive evaluations on both synthetic and real-world datasets with human-level annotations to demonstrate the effectiveness of the proposed methods as well as the parameter selection.

Datasets. We use synthetic data for training, where 400 ultra-high-resolution isotropic scans are generated from created segmentation labels with a resolution of $\frac{1}{3} \text{ mm} \times \frac{1}{3} \text{ mm} \times \frac{1}{3} \text{ mm}$, and the other 100 for validation. For evaluation, we employ two test sets: (1) a synthetic test set comprising 100 held-out synthetic volumes, and (2) 20 real scans from the *U01* dataset¹, each with a single annotated 2D slice. The *U01* surface models were originally generated by converting segmentation probability maps, obtained using a cascaded multi-resolution U-Net [69], into pseudo T1-weighted scans, followed by surface placement using a modified version of the FreeSurfer recon-all pipeline [17, 21]. More details are provided in the supplementary material.

Implementation details. We use a standard 3D UNet [55, 16] as the backbone for our segmentation. The networks are randomly initialized and trained from scratch. We use the Dice loss [61] as segmentation loss and l_1 loss as the consistency loss (if applicable) to supervise the training of the network. Adam optimizer [39] is adopted with a learning rate of 1×10^{-3} . We set the loss weights of λ_{gd} , λ_{tv} , and λ_{cons} as 0.1, 0.01 and 1 for all our experiments except for the ablation study sections regarding these parameters. Note that the reported memory usage corresponds to an input size of $192 \times 192 \times 192$ with a batch size of 1. More information is provided as supplementary material.

Evaluation metrics. We use Dice score [72] and the Hausdorff distance (HD) to report all the performances. The Dice score [72] is a classical segmentation metric, which measures the overlap between predicted and ground truth masks. The Hausdorff distance (HD) [32] calculates the maximum distance between these two boundaries. We report both mean and standard deviations for all the results, and bolded numbers denote significant differences (t-test, $p = 0.05$).

4.1 Supervised Segmentation with Low-Resolution Guidance

We first evaluate the fully supervised segmentation with low-resolution guidance results under different settings.

Results. Table 1 presents the quantitative segmentation results across different experimental settings, while qualitative examples are shown in Figure 3. As observed in the table, incorporating the low-resolution segmentation S_l as spatial guidance significantly enhances performance in both configurations, whether predicting the segmentation map \hat{S}_H directly or regressing the signed distance function (SDF) \hat{D}_H . Notably, regressing \hat{D}_H leads to further improvements over direct segmentation, suggesting that the continuous and boundary-aware nature of distance transforms provides a more effective learning signal. The results are also reflected by the segmentation maps illustrated in Figure 3.

¹<https://dandiarchive.org/dandiset/000026>

Table 1: Segmentation (Seg.) results with different settings.

Method	Guidance	Synthetic dataset		U01	
		Dice \uparrow	HD95 (mm) \downarrow	Dice \uparrow	HD95 (mm) \downarrow
Naive seg. (Section 3.1.1)	N/A	0.754 \pm 0.022	0.886 \pm 0.153	0.721 \pm 0.046	1.471 \pm 0.204
Predict seg. \hat{S}_H (Section 3.1.2)	S_l	0.771 \pm 0.023	0.803 \pm 0.124	0.743 \pm 0.037	1.015 \pm 0.198
Regress SDF \hat{D}_H (Section 3.2)		0.782 \pm 0.015	0.768 \pm 0.106	0.751 \pm 0.026	0.976 \pm 0.151

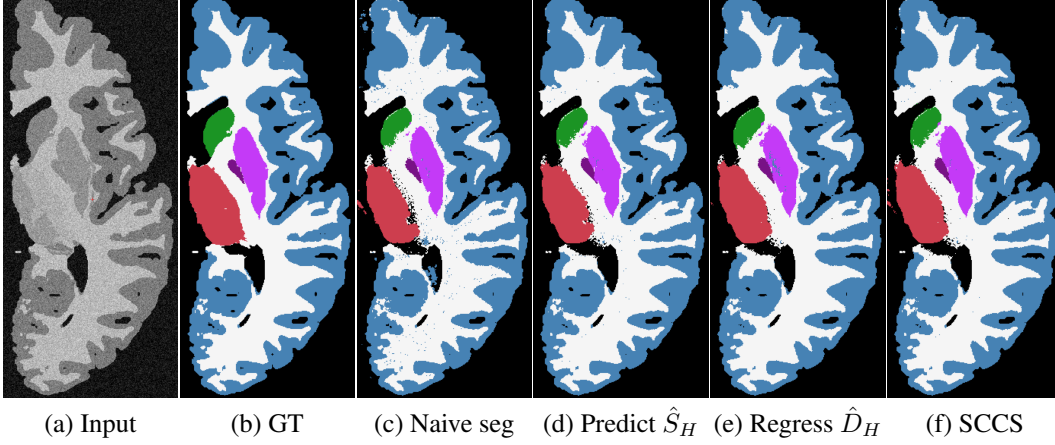


Figure 3: Qualitative results. (a), (b) show the input and segmentation. (c) - (f) show the segmentations of different methods.

4.1.1 Ablation Study

We conduct a series of ablation studies to justify the effectiveness of individual components, as well as the sensitivity of hyperparameters.

Ablation study on the consistency loss term. As mentioned above, beyond using as a spatial guidance, S_l is also used to enforce semantic consistency. To evaluate the contribution of the consistency loss $\mathcal{L}_{\text{cons}}$ in both settings, we conduct ablation experiments by removing $\mathcal{L}_{\text{cons}}$. The results in Table 2 demonstrate that incorporating $\mathcal{L}_{\text{cons}}$ consistently improves segmentation performance.

 Table 2: Ablation study for $\mathcal{L}_{\text{cons}}$.

Method	Setting	Dice \uparrow	HD95 (mm) \downarrow
Predict seg. \hat{S}_H	Seg. as input (w/o $\mathcal{L}_{\text{cons}}$)	0.765 \pm 0.018	0.841 \pm 0.145
	Seg. as input (w/ $\mathcal{L}_{\text{cons}}$)	0.771 \pm 0.023	0.803 \pm 0.124
Regress SDF \hat{D}_H	Seg. as input (w/o $\mathcal{L}_{\text{cons}}$)	0.773 \pm 0.016	0.826 \pm 0.156
	Seg. as input (w $\mathcal{L}_{\text{cons}}$)	0.782 \pm 0.015	0.768 \pm 0.106

Ablation study on the loss components. We further analyze the contribution of each loss component in Equation (5). As shown in Table 3, each loss term individually contributes to improved segmentation accuracy. When combined, these terms yield the best overall performance, confirming that \mathcal{L}_{∇} , \mathcal{L}_{TV} , and $\mathcal{L}_{\text{cons}}$ are complementary to each other and jointly beneficial for the segmentation task.

Table 3: Ablation study on components.

\mathcal{L}_{∇}	\mathcal{L}_{TV}	$\mathcal{L}_{\text{cons}}$	Dice \uparrow	HD95 (mm) \downarrow
\times	\times	\times	0.748 \pm 0.025	1.023 \pm 0.176
\checkmark	\times	\times	0.765 \pm 0.018	0.937 \pm 0.181
\times	\checkmark	\times	0.760 \pm 0.012	0.895 \pm 0.161
\times	\times	\checkmark	0.754 \pm 0.021	1.123 \pm 0.145
\checkmark	\checkmark	\times	0.773 \pm 0.016	0.826 \pm 0.156
\checkmark	\times	\checkmark	0.768 \pm 0.019	0.847 \pm 0.136
\times	\checkmark	\checkmark	0.766 \pm 0.016	0.812 \pm 0.124
\checkmark	\checkmark	\checkmark	0.782 \pm 0.015	0.768 \pm 0.106

Ablation study on loss weights. The sensitivity of the loss weights in Equation (5) is investigated in Table 4, Table 5, and Table 6. The results indicate that the proposed method is quite robust to the choice of loss weight values.

Table 4: Ablation study on λ_{gd} .

λ_{gd}	Dice \uparrow	HD95 (mm) \downarrow
0	0.766 ± 0.016	0.812 ± 0.124
0.05	0.775 ± 0.018	0.826 ± 0.110
<u>0.10</u>	0.782 ± 0.015	0.768 ± 0.106
0.15	0.778 ± 0.021	0.756 ± 0.129
0.20	0.772 ± 0.017	0.801 ± 0.098

Table 5: Ablation study on λ_{lv} .

λ_{gd}	Dice \uparrow	HD95 (mm) \downarrow
0	0.768 ± 0.019	0.847 ± 0.136
0.001	0.765 ± 0.022	0.825 ± 0.101
<u>0.01</u>	0.782 ± 0.015	0.768 ± 0.106
0.02	0.779 ± 0.010	0.771 ± 0.085
0.05	0.766 ± 0.021	0.871 ± 0.123

Table 6: Ablation study on λ_{cons} .

λ_{cons}	Dice \uparrow	HD95 (mm) \downarrow
0	0.773 ± 0.016	0.826 ± 0.156
0.5	0.777 ± 0.021	0.746 ± 0.090
<u>1.0</u>	0.782 ± 0.015	0.768 ± 0.106
1.5	0.781 ± 0.019	0.790 ± 0.141
2.0	0.775 ± 0.017	0.782 ± 0.161

4.2 Scalable Class-Conditional Segmentation (SCCS)

We further conduct experiments to evaluate the effectiveness of the proposed *scalable class-conditional segmentation* strategy.

Comparison with classical multi-class segmentation. Table 7 compares our proposed *scalable class-conditional segmentation* (SCCS) framework against the conventional all-class conditioning setting. While the all-class conditioning method achieves a slightly higher Dice score (0.771 ± 0.023 vs. 0.758 ± 0.017), it does so at the cost of increased GPU memory consumption (3.45 GB vs. 3.18 GB). This memory arises from the need to input all class-conditioning channels simultaneously. In contrast, SCCS processes one class at a time, making it inherently more scalable. As the number of segmentation classes increases, the memory required by all-class conditioning will grow linearly with the number of classes, potentially becoming prohibitive. Therefore, SCCS offers a more memory-efficient alternative, especially valuable in settings involving a large number of anatomical structures or limited computational resources.

Table 7: Comparison between all-class conditioning and scalable class-conditional segmentation.

Method	Input Channels	Dice \uparrow	HD95 \downarrow	Memory (GB)
All-class conditioning	$1 + C$	0.771 ± 0.023	0.803 ± 0.124	3.45 GB
SCCS (Ours)	$1 + 1$	0.758 ± 0.017	0.826 ± 0.142	3.18 GB

Generalization to held-out classes. We conduct another experiment to illustrate the ability of our SCCS framework to generalize to unseen anatomical classes by holding out one class during the training, and the results are shown in Table 8. While the classical model achieves a slightly higher Dice score on seen classes (0.782 ± 0.019 vs. 0.771 ± 0.016), it lacks the flexibility to segment unseen classes without retraining. In contrast, SCCS is designed to process one class at a time using a class-conditional input, allowing it to generalize to new, held-out classes at test time. This flexibility is demonstrated by its reasonable performance on unseen classes (Dice: 0.687 ± 0.036), highlighting the advantage of SCCS in scenarios where the complete label set may evolve or expand over time.

Table 8: Generalization performance on unseen anatomical classes. SCCS enables segmentation of held-out classes without retraining, while the classical model fails to generalize.

Method	Input Channels	Seen Classes (Dice \uparrow)	Unseen Classes (Dice \uparrow)	Memory (GB)
Classical multi-class segmentation	$1 + (C - 1)$	0.782 ± 0.019	N/A	3.42 GB
SCCS (Ours)	$1 + 1$	0.771 ± 0.016	0.687 ± 0.036	3.18 GB

5 Conclusion

In this work, we present a novel framework for brain image segmentation that leverages low-resolution coarse labels as spatial references. By regressing per-class signed distance transform maps instead of directly predicting discrete labels, our method enables smooth, boundary-aware supervision that better captures anatomical geometry. To further improve scalability and generalizability, we introduce a scalable class-conditional segmentation strategy, where the model is trained to segment one class at a time using class-specific input conditioning. This design significantly reduces memory usage during training and supports generalization to unseen anatomical structures. Extensive experiments on both synthetic and real-world datasets validate the effectiveness of our approach, demonstrating consistent improvements in segmentation accuracy, efficiency, and scalability over conventional multi-class segmentation baselines.

References

- [1] Zeynettin Akkus, Alfiia Galimzianova, Assaf Hoogi, Daniel L Rubin, and Bradley J Erickson. Deep learning for brain MRI segmentation: state of the art and future directions. *Journal of digital imaging*, 2017.
- [2] Nicolas Audebert, Alexandre Boulch, Bertrand Le Saux, and Sébastien Lefèvre. Distance transform regression for spatially-aware deep semantic segmentation. *CVIU*, 2019.
- [3] Benjamin Billot, Douglas N Greve, Oula Puonti, Axel Thielscher, Koen Van Leemput, Bruce Fischl, Adrian V Dalca, Juan Eugenio Iglesias, et al. Synthseg: Segmentation of brain mri scans of any contrast and resolution without retraining. *MedIA*, 2023.
- [4] Lea Bogensperger, Dominik Narnhofer, Alexander Falk, Konrad Schindler, and Thomas Pock. Flowsdf: Flow matching for medical image segmentation using distance transforms. *IJCV*, 2025.
- [5] Victor Ion Butoi, Jose Javier Gonzalez Ortiz, Tianyu Ma, Mert R Sabuncu, John Guttag, and Adrian V Dalca. Universeg: Universal medical image segmentation. In *ICCV*, 2023.
- [6] Fabio Cermelli, Massimiliano Mancini, Samuel Rota Buló, Elisa Ricci, and Barbara Caputo. Modeling the background for incremental learning in semantic segmentation. In *CVPR*, 2020.
- [7] Chao Chen, Yu-Shen Liu, and Zhizhong Han. Unsupervised inference of signed distance functions from single sparse point clouds without learning priors. In *CVPR*, 2023.
- [8] Cheng Chen, Qi Dou, Hao Chen, Jing Qin, and Pheng-Ann Heng. Synergistic image and feature adaptation: Towards cross-modality domain adaptation for medical image segmentation. In *AAAI*, 2019.
- [9] Jieneng Chen, Yongyi Lu, Qihang Yu, Xiangde Luo, Ehsan Adeli, Yan Wang, Le Lu, Alan L Yuille, and Yuyin Zhou. Transunet: Transformers make strong encoders for medical image segmentation. *arXiv preprint arXiv:2102.04306*, 2021.
- [10] Liang-Chieh Chen, George Papandreou, Iasonas Kokkinos, Kevin Murphy, and Alan L Yuille. Semantic image segmentation with deep convolutional nets and fully connected crfs. *arXiv preprint arXiv:1412.7062*, 2014.
- [11] Liang-Chieh Chen, George Papandreou, Iasonas Kokkinos, Kevin Murphy, and Alan L Yuille. Deeplab: Semantic image segmentation with deep convolutional nets, atrous convolution, and fully connected crfs. *TPAMI*, 2018.
- [12] Liang-Chieh Chen, George Papandreou, Florian Schroff, and Hartwig Adam. Rethinking atrous convolution for semantic image segmentation. *arXiv preprint arXiv:1706.05587*, 2017.
- [13] Yuanhong Chen, Chong Wang, Yuyuan Liu, Hu Wang, and Gustavo Carneiro. CPM: Class-conditional prompting machine for audio-visual segmentation. In *ECCV*, 2024.
- [14] Julian Chibane, Gerard Pons-Moll, et al. Neural unsigned distance fields for implicit function learning. In *NeurIPS*, 2020.
- [15] Gene Chou, Ilya Chugunov, and Felix Heide. Gensdf: Two-stage learning of generalizable signed distance functions. In *NeurIPS*, 2022.
- [16] Özgün Çiçek, Ahmed Abdulkadir, Soeren S Lienkamp, Thomas Brox, and Olaf Ronneberger. 3D U-Net: learning dense volumetric segmentation from sparse annotation. In *MICCAI*, 2016.
- [17] Anders M Dale, Bruce Fischl, and Martin I Sereno. Cortical surface-based analysis: I. segmentation and surface reconstruction. *Neuroimage*, 1999.
- [18] Ricardo Fabbri, Luciano Da F Costa, Julio C Torelli, and Odemir M Bruno. 2D euclidean distance transform algorithms: A comparative survey. *CSUR*, 2008.
- [19] Aly A Farag, Jasjit S Suri, and George J Grevera. Distance transform algorithms and their implementation and evaluation. *Deformable models: Biomedical and clinical applications*, 2007.
- [20] Ruiwei Feng, Xiangshang Zheng, Tianxiang Gao, Jintai Chen, Wenzhe Wang, Danny Z Chen, and Jian Wu. Interactive few-shot learning: Limited supervision, better medical image segmentation. *TMI*, 2021.
- [21] Bruce Fischl, Martin I Sereno, and Anders M Dale. Cortical surface-based analysis: II: inflation, flattening, and a surface-based coordinate system. *Neuroimage*, 1999.

- [22] Vitaly L Galinsky and Lawrence R Frank. Automated segmentation and shape characterization of volumetric data. *NeuroImage*, 2014.
- [23] Dan Andrei Ganea, Bas Boom, and Ronald Poppe. Incremental few-shot instance segmentation. In *CVPR*, 2021.
- [24] Prachi Garg, Rohit Saluja, Vineeth N Balasubramanian, Chetan Arora, Anbumani Subramanian, and CV Jawahar. Multi-domain incremental learning for semantic segmentation. In *WACV*, 2022.
- [25] Mohsen Ghafoorian, Alireza Mehrtash, Tina Kapur, Nico Karssemeijer, Elena Marchiori, Mehran Pesteie, Charles RG Guttmann, Frank-Erik De Leeuw, Clare M Tempny, Bram Van Ginneken, et al. Transfer learning for domain adaptation in MRI: Application in brain lesion segmentation. In *MICCAI*, 2017.
- [26] Alberto F Goldszal, Christos Davatzikos, Dzung L Pham, Michelle XH Yan, R Nick Bryan, and Susan M Resnick. An image-processing system for qualitative and quantitative volumetric analysis of brain images. *JCAT*, 1998.
- [27] Amos Gropp, Lior Yariv, Niv Haim, Matan Atzmon, and Yaron Lipman. Implicit geometric regularization for learning shapes. *arXiv preprint arXiv:2002.10099*, 2020.
- [28] Endre Grøvik, Darvin Yi, Michael Iv, Elizabeth Tong, Daniel Rubin, and Greg Zaharchuk. Deep learning enables automatic detection and segmentation of brain metastases on multisequence MRI. *JMRI*, 2020.
- [29] Mohammad Havaei, Axel Davy, David Warde-Farley, Antoine Biard, Aaron Courville, Yoshua Bengio, Chris Pal, Pierre-Marc Jodoin, and Hugo Larochelle. Brain tumor segmentation with deep neural networks. *MedIA*, 2017.
- [30] Kaiming He, Xiangyu Zhang, Shaoqing Ren, and Jian Sun. Deep residual learning for image recognition. In *CVPR*, 2016.
- [31] Leonie Henschel, Sailesh Conjeti, Santiago Estrada, Kersten Diers, Bruce Fischl, and Martin Reuter. Fastsurfer-a fast and accurate deep learning based neuroimaging pipeline. *NeuroImage*, 2020.
- [32] Daniel P Huttenlocher, Gregory A. Klanderman, and William J Rucklidge. Comparing images using the Hausdorff distance. *TPAMI*, 1993.
- [33] George W Hynd, Margaret Semrud-Clikeman, Alison R Lorys, Edward S Novey, Deborah Eliopoulos, and Heikki Lyytinen. Corpus callosum morphology in attention deficit-hyperactivity disorder: morphometric analysis of MRI. *Journal of Learning Disabilities*, 1991.
- [34] Juan Eugenio Iglesias and Mert R Sabuncu. Multi-atlas segmentation of biomedical images: a survey. *MedIA*, 2015.
- [35] Fabian Isensee, Paul F Jaeger, Simon AA Kohl, Jens Petersen, and Klaus H Maier-Hein. nnu-net: a self-configuring method for deep learning-based biomedical image segmentation. *Nature methods*, 2021.
- [36] Yue Jiang, Dantong Ji, Zhizhong Han, and Matthias Zwicker. Sdfdiff: Differentiable rendering of signed distance fields for 3D shape optimization. In *CVPR*, 2020.
- [37] Konstantinos Kamnitsas, Christian Ledig, Virginia FJ Newcombe, Joanna P Simpson, Andrew D Kane, David K Menon, Daniel Rueckert, and Ben Glocker. Efficient multi-scale 3D CNN with fully connected crf for accurate brain lesion segmentation. *MedIA*, 2017.
- [38] Pulkit Khandelwal, Michael Tran Duong, Shokufeh Sadaghiani, Sydney Lim, Amanda E Denning, Eunice Chung, Sathana Ravikumar, Sanaz Arezoumandan, Claire Peterson, Madigan Bedard, et al. Automated deep learning segmentation of high-resolution 7 tesla postmortem MRI for quantitative analysis of structure-pathology correlations in neurodegenerative diseases. *Imaging Neuroscience*, 2024.
- [39] Diederik P Kingma and Jimmy Ba. Adam: A method for stochastic optimization. *arXiv preprint arXiv:1412.6980*, 2014.
- [40] Alexander Kirillov, Ross Girshick, Kaiming He, and Piotr Dollár. Panoptic feature pyramid networks. In *CVPR*, 2019.
- [41] Alexander Kirillov, Eric Mintun, Nikhila Ravi, Hanzi Mao, Chloe Rolland, Laura Gustafson, Tete Xiao, Spencer Whitehead, Alexander C Berg, Wan-Yen Lo, et al. Segment anything. In *ICCV*, 2023.
- [42] Alex Krizhevsky, Ilya Sutskever, and Geoffrey E Hinton. Imagenet classification with deep convolutional neural networks. In *NeurIPS*, 2012.

- [43] Junjie Liang, Cihui Yang, Jingting Zhong, and Xiaoli Ye. BTSwin-Unet: 3D U-shaped symmetrical swin transformer-based network for brain tumor segmentation with self-supervised pre-training. *Neural processing letters*, 2023.
- [44] T Logeswari and M Karnan. An improved implementation of brain tumor detection using segmentation based on soft computing. *Journal of Cancer Research and Experimental Oncology*, 2010.
- [45] Jonathan Long, Evan Shelhamer, and Trevor Darrell. Fully convolutional networks for semantic segmentation. In *CVPR*, 2015.
- [46] Baorui Ma, Junsheng Zhou, Yu-Shen Liu, and Zhizhong Han. Towards better gradient consistency for neural signed distance functions via level set alignment. In *CVPR*, 2023.
- [47] Jun Ma, Zhan Wei, Yiwen Zhang, Yixin Wang, Rongfei Lv, Cheng Zhu, Chen Gaoxiang, Jianan Liu, Chao Peng, Lei Wang, et al. How distance transform maps boost segmentation cnns: an empirical study. In *MIDL*, 2020.
- [48] Gloria P Mazzara, Robert P Velthuizen, James L Pearlman, Harvey M Greenberg, and Henry Wagner. Brain tumor target volume determination for radiation treatment planning through automated MRI segmentation. *International Journal of Radiation Oncology, Biology, Physics*, 2004.
- [49] Fausto Milletari, Nassir Navab, and Seyed-Ahmad Ahmadi. V-net: Fully convolutional neural networks for volumetric medical image segmentation. In *3DV*, 2016.
- [50] Hyeonwoo Noh, Seunghoon Hong, and Bohyung Han. Learning deconvolution network for semantic segmentation. In *ICCV*, 2015.
- [51] Stanley Osher, Ronald Fedkiw, Stanley Osher, and Ronald Fedkiw. Constructing signed distance functions. *Level set methods and dynamic implicit surfaces*, 2003.
- [52] Cheng Ouyang, Carlo Biffi, Chen Chen, Turkay Kart, Huaqi Qiu, and Daniel Rueckert. Self-supervised learning for few-shot medical image segmentation. *TMI*, 2022.
- [53] Jeong Joon Park, Peter Florence, Julian Straub, Richard Newcombe, and Steven Lovegrove. DeepSDF: Learning continuous signed distance functions for shape representation. In *CVPR*, 2019.
- [54] Ramin Ranjbarzadeh, Abbas Bagherian Kasgari, Saeid Jafarzadeh Ghouschi, Shokofeh Anari, Maryam Naseri, and Malika Bendechache. Brain tumor segmentation based on deep learning and an attention mechanism using MRI multi-modalities brain images. *Scientific reports*, 2021.
- [55] Olaf Ronneberger, Philipp Fischer, and Thomas Brox. U-net: Convolutional networks for biomedical image segmentation. In *MICCAI*, 2015.
- [56] Azriel Rosenfeld and John L Pfaltz. Distance functions on digital pictures. *Pattern Recognition (PR)*, 1968.
- [57] Abhijit Guha Roy, Sailesh Conjeti, Nassir Navab, Christian Wachinger, Alzheimer’s Disease Neuroimaging Initiative, et al. Quicknat: A fully convolutional network for quick and accurate segmentation of neuroanatomy. *NeuroImage*, 2019.
- [58] Mert R Sabuncu, BT Thomas Yeo, Koen Van Leemput, Bruce Fischl, and Polina Golland. A generative model for image segmentation based on label fusion. *TMI*, 2010.
- [59] Punam K Saha, Felix W Wehrli, and Bryon R Gomberg. Fuzzy distance transform: theory, algorithms, and applications. *CVIU*, 2002.
- [60] Karen Simonyan and Andrew Zisserman. Very deep convolutional networks for large-scale image recognition. *arXiv preprint arXiv:1409.1556*, 2014.
- [61] Carole H Sudre, Wenqi Li, Tom Vercauteren, Sebastien Ourselin, and M Jorge Cardoso. Generalised dice overlap as a deep learning loss function for highly unbalanced segmentations. In *DLMIA*, 2017.
- [62] Weixuan Sun, Jing Zhang, and Nick Barnes. Inferring the class conditional response map for weakly supervised semantic segmentation. In *WACV*, 2022.
- [63] Christian Szegedy, Wei Liu, Yangqing Jia, Pierre Sermanet, Scott Reed, Dragomir Anguelov, Dumitru Erhan, Vincent Vanhoucke, and Andrew Rabinovich. Going deeper with convolutions. In *CVPR*, 2015.
- [64] Hao Tang, Xingwei Liu, Shanlin Sun, Xiangyi Yan, and Xiaohui Xie. Recurrent mask refinement for few-shot medical image segmentation. In *ICCV*, 2021.

- [65] M Vaidyanathan, Laurence P Clarke, LO Hall, C Heidtman, R Velthuisen, K Gosche, S Phuphanich, H Wagner, H Greenberg, and ML Silbiger. Monitoring brain tumor response to therapy using MRI segmentation. *Magnetic resonance imaging*, 1997.
- [66] Vanya V Valindria, Nick Pawlowski, Martin Rajchl, Ioannis Lavdas, Eric O Aboagye, Andrea G Rockall, Daniel Rueckert, and Ben Glocker. Multi-modal learning from unpaired images: Application to multi-organ segmentation in CT and MRI. In *WACV*, 2018.
- [67] Koen Van Leemput, Frederik Maes, Dirk Vandermeulen, and Paul Suetens. A unifying framework for partial volume segmentation of brain MR images. *TMI*, 2003.
- [68] Yan Wang, Xu Wei, Fengze Liu, Jieneng Chen, Yuyin Zhou, Wei Shen, Elliot K Fishman, and Alan L Yuille. Deep distance transform for tubular structure segmentation in CT scans. In *CVPR*, 2020.
- [69] Xiangrui Zeng, Oula Puonti, Areej Sayeed, Rogeny Herisse, Jocelyn Mora, Kathryn Evancic, Divya Varadarajan, Yael Balbastre, Irene Costantini, Marina Scardigli, et al. Segmentation of supragranular and infragranular layers in ultra-high-resolution 7T ex vivo MRI of the human cerebral cortex. *Cerebral Cortex*, 2024.
- [70] Jiaying Zhang, Guibo Luo, Zi’Ang Zhang, and Yuesheng Zhu. Data augmentation in class-conditional diffusion model for semi-supervised medical image segmentation. In *IJCNN*, 2024.
- [71] Zongwei Zhou, Vatsal Sodha, Md Mahfuzur Rahman Siddiquee, Ruibin Feng, Nima Tajbakhsh, Michael B Gotway, and Jianming Liang. Models genesis: Generic autodidactic models for 3D medical image analysis. In *MICCAI*, 2019.
- [72] Kelly H Zou, Simon K Warfield, Aditya Bharatha, Clare MC Tempany, Michael R Kaus, Steven J Haker, William M Wells III, Ferenc A Jolesz, and Ron Kikinis. Statistical validation of image segmentation quality based on a spatial overlap index 1: scientific reports. *Academic radiology*, 2004.

6 Overview

In the supplementary material, we begin with the details of the datasets Section 7, followed by the implementation details in Section 8. Then, we provide the computational resources in Section 9, followed by a few other qualitative samples in Section 10. The limitations are provided in Section 11, followed by an analysis on the broader impact in Section 12.

7 Dataset Details

Synthetic data. As described in the main text, we use synthetic data for training. The ultra-high-resolution isotropic scans are generated from created segmentation labels at a resolution of $\frac{1}{3}$ mm \times $\frac{1}{3}$ mm \times $\frac{1}{3}$ mm. The coarse, low-resolution segmentation S_l is obtained using SynthSeg [3], which segments approximately 30 brain regions at 1 mm isotropic resolution, regardless of the input resolution. We group these regions into 7 foreground classes, *Cortex*, *White Matter*, *Thalamic Mask*, *Pallidum Mask*, *Putamen Mask*, *Caudate and Accumbens*, and *Cerebellar Gray Matter*, along with a background class. The detailed mapping list will be provided to ensure reproducibility.

Real data. Following the same class grouping used for the synthetic data, we asked expert annotators to manually label one representative slice from each of 20 real scans in the *U01* dataset².

8 Implementation Details

Network details. The 3D UNet architecture employed in this paper follows an encoder-decoder structure with skip connections, designed to capture both global context and fine-grained spatial details in volumetric medical images. The encoder consists of four downsampling blocks, each composed of two 3D convolutional layers followed by batch normalization and LeakyReLU activations, with 3D max pooling used to progressively reduce spatial resolution while increasing the number of feature channels. The bottleneck (or bridge) layer connects the encoder and decoder, maintaining the deepest representation with the highest channel dimension. The decoder mirrors the encoder with four upsampling blocks, where each block begins with a transposed 3D convolution to upsample the feature map, followed by concatenation with the corresponding encoder features (skip connection), and two additional convolutional layers with normalization and activation. The final output layer is a 3D convolution that maps the feature maps to the desired number of output channels. This design enables precise voxel-wise predictions while maintaining spatial consistency across the 3D volume. The codes will be released upon acceptance to ensure reproducibility.

9 Computational Resources

The experiments are conducted on an NVIDIA A40 GPU (48GB), using a 26-core Intel(R) Xeon(R) Gold 6230R CPU @ 2.10GHz and 200 GB RAM.

10 Qualitative Results

For qualitative results, we provide another sample from *U01* in Figure 4.

11 Limitations

A key limitation of the proposed method lies in its reliance on automatic low-resolution segmentations as spatial guidance. While this strategy significantly reduces manual labeling effort, it inherently assumes that these coarse labels are accurate and spatially consistent. In practice, however, these low-resolution segmentations may contain systematic biases or anatomical imprecision. These imperfections can propagate through the network, potentially leading to degraded segmentation performance at higher resolutions. One possible solution is to incorporate uncertainty modeling

²<https://dandiarchive.org/dandiset/000026>

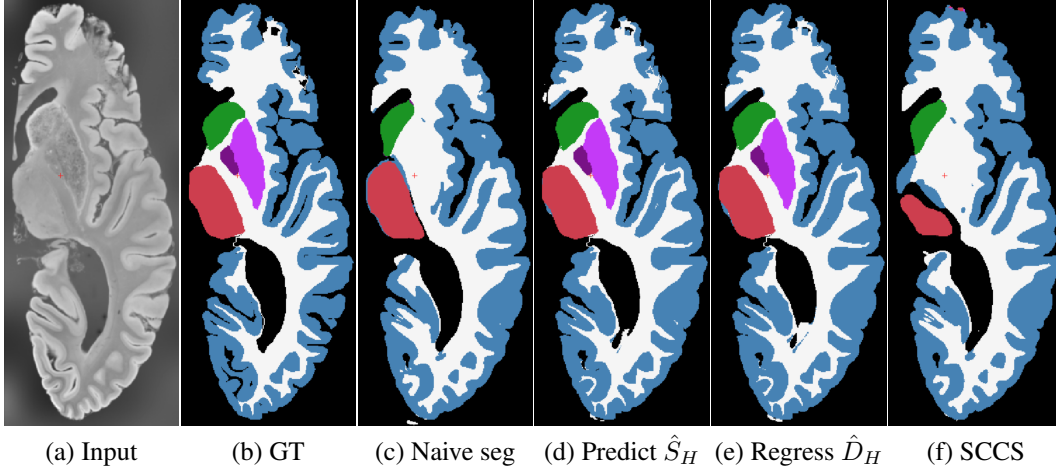


Figure 4: Qualitative results. (a), (b) show the input and segmentation. (c) - (f) show the segmentations of different methods.

or confidence-weighted supervision, where the model learns to discount or correct for less reliable regions in the coarse labels. Additionally, leveraging self-supervised refinement mechanisms that iteratively improve the alignment between low- and high-resolution outputs could further mitigate this issue.

Another important limitation is the limited validation on real, fully annotated 3D clinical datasets. Although the paper demonstrates strong performance on synthetic data and sparsely labeled real data (e.g., single-slice annotations), the generalizability of the proposed approach to densely annotated, high-resolution clinical scans remains uncertain. This is particularly relevant given the variability in acquisition protocols, scanner hardware, and anatomical differences across patient populations. To strengthen the empirical evidence and assess robustness, future work should include comprehensive benchmarking on public and private datasets with full volumetric annotations (e.g., HCP, OASIS, ADNI). Incorporating domain adaptation techniques or semi-supervised learning frameworks could also help bridge the gap between synthetic and clinical domains, further enhancing the method’s practical utility in real-world settings.

12 Broader Impact

The broader impact of our work lies in its potential to democratize access to detailed, high-fidelity brain image analysis without the prohibitive cost of dense manual annotations. By leveraging low-resolution coarse labels and a scalable, class-conditional framework, the proposed method makes it feasible to segment ultra-high-resolution brain MR scans, which are increasingly used in neuroscience and clinical research, using limited supervision and computational resources. This can accelerate research in neurodegenerative diseases, brain development, and population-level studies where large-scale, accurate segmentation is essential.

Additionally, the framework’s ability to generalize to unseen classes and operate efficiently in memory-constrained settings makes it adaptable to low-resource clinical environments or global health applications. However, as with any medical AI tool, careful validation is essential to avoid biases or errors introduced by synthetic or weak labels. If responsibly developed and adopted, the method could contribute meaningfully to advancing scalable, accessible, and precise neuroimaging analysis.